Spin Dynamics in Spintronic Devices: A Growing Science in Microwave Applications

John Q. Xiao[1,2], CAO Rong [1], Moriyama T [1], FAN Xing[1], WEN Qi-ye[2] and ZHANG Hai-wu[2]

(1. Department of Physics and Astronomy, University of Delaware Newark USA 19716

2. State Key Laboratory of Electronic Films and Integrated Devices, University of Electronic Science and Technology of China Chengdu 610054)

Abstract The spintronics refers to the research area where electron spins, in additional to or sometimes in place of electron charges, are controlled and manipulated to give rise to an array of properties. Spintronic devices have already found applications in computer hard drive and magnetic random access memory, profoundly changed the information technology industry. These applications utilize the spin polarized transport where electron with fixed spin direction transverse through magnetic heterostructures. More recently, investigation of spin dynamics in spintronic device relates microwave with spin polarized transport, offering significant potential for novel microwave devices with dimension far less than the microwave wavelength. In this "review-like" article, we first briefly introduce the concept of spintronic devices. Microwave experiments with spintronic devices are discussed next in the context of microwave assisted switching and spin pumping phenomenon. The former has potential for developing high density computer hard disk, the latter, with the development of direct electronic detection, could lead to miniaturized and passive microwave detector.

Key words heterojunctions; microwave measurements; spin dynamics; spin pumping

自旋器件中的自旋动力学：微波领域应用的新兴科学

肖 强[1,2]，曹 荣[1]，MORIYAMA T[1]，范 欣[1]，文岐业[2]，张怀武[2]

(1. 特拉华大学物理与天文学院 纽瓦克市 美国 19716; 2. 电子科技大学电子薄膜与集成器件国家重点实验室 成都 610054)

【摘要】自旋电子学指通过控制和利用电子自旋(而不是电荷)获得一系列新颖性能的研究领域。自旋电子器件已经成功地应用于计算机硬盘驱动器和磁性随机存储器，对IT行业的发展产生了深远的影响。这些应用都是基于自旋极化传输效应，即具有固定自旋取向的电子穿过磁性异质结所发生的相关效应。目前，在将微波和自旋极化传输联系起来的自旋器件中的自旋动力学研究，为研制尺寸远远小于微波波长的新型微波器件提供了巨大的潜能。在这篇综述中，首先简单地介绍了自旋器件的概念；接着研究了微波实验来研究自旋电子器件的微波辅助翻转和自旋泵浦现象。前者将能够开发出高密度的计算机硬盘，而后者，结合直接电子检测技术，将能够实现小型化的无源微波探测器。

关 键 词 异质结; 微波测量; 自旋动力学; 自旋泵浦效应

中图分类号 O441.2; TM27 **文献标识码** A doi:10.3969/j.issn.1001-0548.2009.05.004

1 Introduction to spintronics

The spintronics refers to the research area where electron spins, in additional to or sometimes in place of electron charges, are controlled and manipulated to give rise to an array of properties. These spintronic properties are typically accompanied by a spin polarized current arisen from the imbalance of spin-up or spin-down electrons at the Fermi level, resulting in a net spin direction associated with the spin polarized current. Ferromagnetic materials are often used to produce a spin-polarized current, which can be maintained throughout the ferromagnetic materials, As the spin-polarized current is injected into nonmagnetic

Received date：2009 – 06 – 30
收稿日期：2009 – 06 – 30
Foundation item：Supported by National Basic Research Program (973) of China(2007CB310407); National Natural Science Foundation of China (60721001, 60801023)
基金项目：国家自然科学基金创新群体(60721001, 60801023); 国家重大基础研究973项目(2007CB310407)

Biofraphy：John Q. Xiao, Full professor of Delaware University, Visiting Professor of Changjiang Scholar of UESTC. Research interesting including spintronics, microwave materials and devices, condensed physics.
作者简介：肖 强(1962 –)，男，美国Delaware大学教授，博士生导师，电子科技大学长江学者讲座教授，主要从事自旋电子学、微波材料与器件、凝聚态物理学方面的研究.

materials, the spin-polarized current is relaxed after a characteristic length known as spin diffusion length. Making an analogy to optics, an Ferromagnetic (FM) material behaves like a polarizer to light. Such a polarization can be detected with a second polarizer, in spintronic devices, a second FM layer.

One important spin-polarized transport phenomenon is the giant magnetoresistance effect (GMR). Fig. 1 shows a typical magnetoresistance measurement with current perpendicular to the plane (CPP) geometry in a spin valve structure, in which two ferromagnetic layers are separated by a nonmagnetic spacer such as Cu. As the relative orientation of the magnetizations in two ferromagnetic layers changes from parallel (P state) to antiparallel (AP state), the resistance of the spin valve changes from low to high values, respectively. This GMR effect can be generally explained within the two-current model[1].

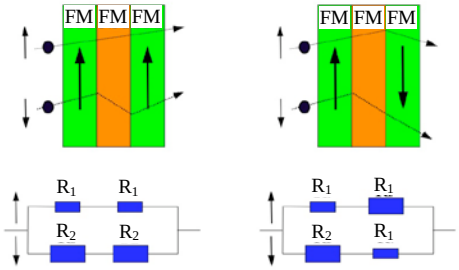

a. parallel magnetizations b. anti-parallel magnetizations

Fig. 1 Electron conduction channels and the corresponding equivalent circuits for a spin valve structure

The key assumption of the two-current model is that the electrical conductivity in metals can be described in terms of two largely independent conducting channels, corresponding to the spin-up and spin-down electrons. These two channels have different resistances due to the spin-dependent electron scattering. Electrons with spin polarization parallel/ antiparallel to the magnetization pass through the structure with little/large scattering, resulting in low/high resistance R_1/R_2. As shown in Fig.1b, when the magnetizations of two magnetic layers are antiparallel, the spin-up electrons have a low resistance R_1 in the first FM layer and a high resistance R_2 in the second FM layer. The opposite happens to the spin-down electrons where a high resistance R_2 is followed by a low resistance R_1. Therefore, both spin-up and spin-down electrons have the same series resistance R_1+ R_2. Then the total resistance in an antiparallel state is:

$$R_{AP} = \frac{(R_1 + R_2)}{2} \tag{1}$$

Following the same argument, the total resistance in a parallel state (Fig.1a) is:

$$R_P = \frac{2R_1R_2}{(R_1 + R_2)} \tag{2}$$

The corresponding GMR in spin valve structures is defined as:

$$M_R = \frac{\Delta R}{R_P} = \frac{R_{AP} - R_P}{R_P} = \frac{(R_2 - R_1)^2}{4R_1R_2} \tag{3}$$

The simplified two-current model discussed here only considers elastic scattering where energy is conserved. Spin-flip scattering is ignored. Spin-flip processes mix up and down spin channels and essentially deteriorate the GMR effect. More discussion on spin-flip process can be found in many sources such as Ref. [2].

Another important spin-polarized transport phenomenon is spin-dependent tunneling, the origin of tunneling magnetoresistance (TMR) found in magnetic tunneling junctions (MTJs). TMR occurs when a current flows between two ferromagnetic layers separated by a thin insulating spacer, about a nanometer thick. The total resistance is dominated by the tunneling process and changes with the relative orientation of magnetizations of the two FM layers. The phenomena are similar to GMR, although with completely different mechanisms.

Michel Julliere, using iron as the ferromagnetic layer and germanium as the insulator, discovered TMR in 1975[3]. Julliere's model took into account only the spin polarizations of each electrode and imposed strict spin conservation across the tunnel barrier so that the tunnel current can simply be related to the product of initial and final density of states for spin-up and spin-down electrons at the Fermi level. The resistances for P and AP configurations are:

$$R_P \propto \frac{V}{D_1^m D_2^m + D_1^M D_2^M} \tag{4}$$

$$R_{AP} \propto \frac{V}{D_1^m D_2^M + D_1^M D_2^m} \tag{5}$$

where D is the density of states. The subscripts 1 and 2 refer to two ferromagnetic electrodes. The superscript m and M stand for minority and majority spin. Assuming the two electrodes are the same:

$$\begin{aligned} D_{1,2}^{m} &= D^{m} \\ D_{1,2}^{M} &= D^{M} \end{aligned} \tag{6}$$

Then

$$M_{\mathrm{R}} = \frac{\Delta R}{R_{\mathrm{P}}} = \frac{2\dfrac{(D^{M}-D^{m})^{2}}{(D^{M}+D^{m})^{2}}}{\dfrac{(D^{M}+D^{m})^{2}}{(D^{M}+D^{m})^{2}} - \dfrac{(D^{M}-D^{m})^{2}}{(D^{M}+D^{m})^{2}}} = \frac{2P^{2}}{1-P^{2}} \tag{7}$$

where $P = \dfrac{(D^{M}-D^{m})}{(D^{M}+D^{m})}$ is the spin polarization of an FM electrode.

In the case that the spin polarizations of the two electrodes are unequal (the densities of states are different), the result is simply generalized to

$$M_{\mathrm{R}} = \frac{2P_{1}P_{2}}{1-P_{1}P_{2}} \tag{8}$$

Following the discovery of GMR effect, room temperature TMR was discovered in 1995, first by Miyazaki and then independently by Refs. [4-5]. It is now the basis for the magnetic random access memory (MRAM) and read heads in hard disk drives. In 2001 Butler and Mathon[6-7] independently proposed that the TMR can reach several thousand percent using Fe/MgO/Fe MTJs. The key to the TMR enhancement here is to use band structure symmetry to create nearly 100% spin polarization. The majority and minority spin bands of Fe have Δ_1 and Δ_2 symmetries, respectively. The electronic bands with Δ_2 symmetry decays much rapidly compared with 1 symmetry inside the crystalline MgO barrier. Consequently, MgO barrier of a nanometer thick can effectively filter out the minority electrons with Δ_2 symmetry, leading to TMR value only expected in MTJs with half metallic electrodes.

2 Spin dynamics and its applications

In 1996, Slonczewski[8] and Berger[9]predicted that the spin polarized current flowing through a magnetic multilayer could exert a spin-transfer torque on the magnetizations in the device, which led to magnetization precession and even reversal if the current density was large enough. In addition to the scientific interests in this phenomenon, it has several important applications such as MRAM. The possibility that spin-transfer torque could replace the conventional coil-generated magnetic fields (Ampere field) for reversing magnetic configurations in MRAM has inspired a significant amount of research in this area. On the other hand, the demand for high-speed devices is pushing the working frequency to GHz range, close to the characteristic precessing frequency of magnetization, known as ferromagnetic resonance, in ferromagnetic materials. The discovery of new phenomena of high frequency spin dynamics in multilayer structures, including MTJs and spin valves, opens the door for new spintronics devices where new functionalities can be achieved.

Although local magnetization dynamics has been studied for a long time and the famous Landau-Lifshitz-Gilbert equation describes the mechanism well, there are still some un-answered questions. For example, a complete theoretical description of the magnetic damping is still missing[10]. Also not fully understood is spin wave excitation in magnetic thin films, which has become a hot topic recently due to the newly proposed “spin wave bus”[11]. Furthermore, nonlinear local magnetization dynamics leads to microwave assisted magnetization reversal[12]. This phenomenon occurs due to a nonlinear magnetization dynamics induced by a high-power time-dependent magnetic field. Microwave assisted magnetization reversal has a potential to replace the current “heat assisted magnetization reversal” technique in magnetic data storage devices, such as HDD and MRAM. The direct interaction between the magnetization and the RF magnetic field is more efficient for reversing the magnetization than the conventional field.

In recent years, many experiments involving nonlocal magnetization dynamics have been performed. The “nonlocal” phenomenon refers to a precessing magnetization in an FM layer interacts with neighboring layers via itinerary electron spins. Nonlocal magnetization dynamics consists of two different effects: (1) current induced spin-transfer torque(STT), and (2) spin pumping where a spin

current is generated by the magnetization precession.

In the first effect, the spin-polarized current driven by an external bias transfers the spin angular momentum through magnetic multilayer and results in a torque on a magnetization. This torque precesses the magnetization and could even reverse the magnetization if the current density is high enough. When STT is coupled with the tunnel magnetoresistance (TMR), the motion of the free layer causes an oscillatory microwave frequency voltage to develop across the MTJ. Thus, a spin transfer oscillator (STO) can be developed to generate microwave signal under a DC bias[13]. Due to its nano-size, the power output of an individual STO is very small. However the power output of an array of N phase-locked oscillators is expected to vary as N^2 [14]. Comparing to the conventional LC oscillator, STO can have much smaller size and greater frequency tunability.

In the spin pumping effect, the precessing magnetization of a ferromagnetic layer pumps spins into adjacent normal metal layers in the absence of electrical bias. An external RF field is used to provide the steady magnetization precession under the ferromagnetic resonance condition. Spin pumping effect is a promising candidate for realizing a spin battery device as a source of pure spin currents where no net charge current is generated[15].

Recently, we proposed a new type of spintronic device-microwave detector[16]. The MTJ based device can be used to analyze the frequency and phase information of microwave signals. This nano-scale microwave detector is superior for device integration and could be the crucial part of the future microwave analyzer.

3 Microwave measurement setup

3.1 Coplanar waveguide

The term “coplanar” is used for transmission lines where all the conductors are in the same plane, namely, on the top surface of a dielectric substrate. One of the advantages of a coplanar waveguide (CPW) is its planar structure, which allows us to fabricate or place thin film devices close to the waveguide. Fig. 2 shows a typical CPW on a dielectric material (substrate). CPW usually consists of a signal line and two grounded lines that are made of conductive materials such as gold and copper.

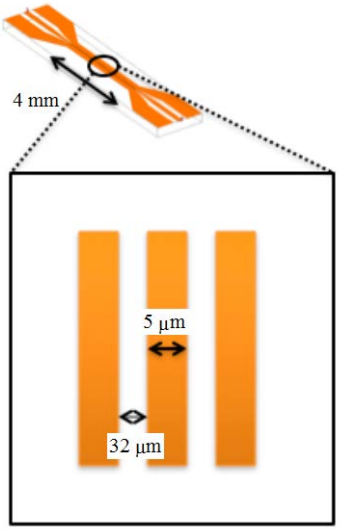

Fig. 2 Schematic of a CPW on a dielectric substrate of finite thickness

Impedance matching is critical to achieve a high transmission through CPWs by reducing the reflection at the interface between CPW and its connectors. It must be designed carefully before the experiment. The geometry of a CPW and the properties of substrate materials determine the impedance of the CPW. Since 50 Ω are used in most microwave instruments and cables, it is necessary to maintain the characteristic impedance of CPWs at 50 Ω as well. Several approaches are used to calculate the impedance of CPWs, including the conformal mapping method (quasi-static analysis), HFSS simulation (fullwave simulation), and AppCAD from Agilent.

In the conformal mapping analysis [17], the CPW conductor and the dielectric material are assumed to have ideal conductivity and relative permittivity (no losses), respectively. Hence the structure is considered to be lossless. All the dielectric interfaces in the structure could be replaced by magnetic walls[18]. Under the above assumption, half-planes above and below the metallic plane of the structure can be analyzed separately for line capacitance. The total capacitance is then the sum of the two capacitances. The effective permittivity ε_{eff} and impedance Z_0 of a CPW can be written as:

$$\varepsilon_{\text{eff}} = \frac{C}{C^a} \tag{9}$$

$$Z_0 = \frac{1}{c\sqrt{\varepsilon_{\text{eff}}}C^a} \tag{10}$$

where c is the speed of electromagnetic waves in free space, C is the total capacitance per unit length of the coplanar line, and C^a is the capacitance of the corresponding line with all the dielectrics replaced by air.

The detailed analysis of the conformal mapping method can be found in Ref. [17]. For the CPW structure used in this work, both the dielectric substrate and the ground planes have finite dimensions. The total capacitance C of the CPW can be calculated as:

$$C = 2\varepsilon_0(\varepsilon_r - 1)\frac{K(k_1)}{K(k_1^+)} + 4\varepsilon_0\frac{K(k_0)}{K(k_0^+)} \tag{11}$$

and the capacitance C^a is:

$$C^a = 4\varepsilon_0\frac{K(k_0)}{K(k_0^+)} \tag{12}$$

where $K(k)$ is the complete elliptic integrals①, and k^+ is defined as:

$$k^+ = \sqrt{1-k^2} \tag{13}$$

Using Eqs. (9) and (10), the effective permittivity ε_{eff} and impedance Z_0 for the CPW in this work (schematically shown in Fig. 2) can be obtained as:

$$\varepsilon_{\text{eff}} = 1 + \frac{(\varepsilon_s - 1)}{2}\frac{K(k_1)}{K(k_1^+)}\frac{K(k_0^+)}{K(k_0)} \tag{14}$$

and

$$Z_0 = \frac{30\pi}{\sqrt{\varepsilon_{\text{eff}}}}\frac{K(k_0^+)}{K(k_0)} \tag{15}$$

where ε_s is the relative permittivity of the dielectric substrate and c is the velocity of the light in free space. With Eqs. (14) and (15), a CPW with $Z_0 = 50\ \Omega$ can be designed by controlling its geometry if the permittivity of the dielectric substrate is known.

Another way to design a CPW is using a High Frequency Structure Simulator (HFSS) program from Ansoft. It is based on tangential vector finite elements, and provides a direct and iterative matrix solver and Eigenmode matrix solver. HFSS is capable of using an incident field from several sources, including a small current loop, dipoles and arbitrary plane waves. It also includes skin effect, loss, frequency dependence, and other parameter inputs for new materials. S parameters, far-field calculation, port mode, impedance, material losses, and radiation losses all could be obtained through HFSS simulation. One advantage of using HFSS is its capability to add any structures on the top of the CPW signal line, which is very useful for designing electronic microwave devices such as a filter. The transmission or reflection properties obtained by HFSS can directly help the design by optimizing different parameters such as direction and magnitude of the external DC magnetic bias.

Besides the above two methods to accurately design the proper CPW for our researches, Agilent AppCAD also provides an alternate way to quickly calculate the impedance of CPWs within reasonable error. The details of this method will be discussed later in this work.

3.2 Ferromagnetic resonance (FMR) measurement

FMR measurement is an indispensible tool for studying spin dynamics in various magnetic materials, especially for magnetic thin films that are widely used in current industry. In traditional FMR measurement, the sample is placed next to the wall of a microwave resonant cavity. A microwave signal at the fixed frequency is fed into the cavity while an external DC magnetic field is applied to the sample. The intensity of the DC magnetic field applied perpendicular to the H vector of the microwave is increased gradually while a microwave detector is set at the end of the cavity to measure the transmission of the microwave through the sample. When the intensity of the DC magnetic field reaches the value that satisfies the FMR condition, the significantly increasing absorption of the microwave in the sample is counteracted with a rapid decrease of the transmission in the detector. While the traditional set-ups are usually bulky and costly, and not easy for electrical measurement on the sample simultaneously, an alternate method called the flip-chip method was opted recently for FMR measurement [19]. The network analyzer measures the S parameters that determine the

① The complete elliptical integral is generally defined as $K(k) = \int_0^{\pi/2} \frac{\mathrm{d}\theta}{\sqrt{1-k^2\sin^2\theta}}$

permittivity and permeability of the sample. The FMR signal is obtained through the permeability profile by analyzing the imaginary part.

In this work, the flip-chip measurement is used to analyze FMR spectra, as depicted in Fig.3. The useful information such as the resonance peak positions and the peak line widths are derived based on the spectra. A CPW with 50 Ω characteristic impedance and an Agilent 8722ES vector network analyzer (VNA) are used for the flip-chip measurement. A 1 cm long CPW is mechanically contacted with the center pin of the SMA connectors at both ends and the whole CPW is placed on the brass housing that is connected to the CPW ground lines. The sample is flipped over and faced down on the CPW. The VNA connected to the CPW through coaxial connectors measures the *S* parameters, including transmission (S_{12}, S_{21}) and reflection (S_{11}, S_{22}). The FMR spectra are taken at constant frequencies while a sweeping external magnetic field is applied along the CPW lines. Then the susceptibility $\chi(H)$ is obtained by a combination of *S* parameters, a constant related to the thickness, the length of the magnetic films, and the characteristic impedance of the CPW. Most information on the FMR can be derived with the imaginary part of susceptibility $\chi''(H)$. In those cases, the absolute value of susceptibility is not needed for analyzing FMR, simplifying the derivation.

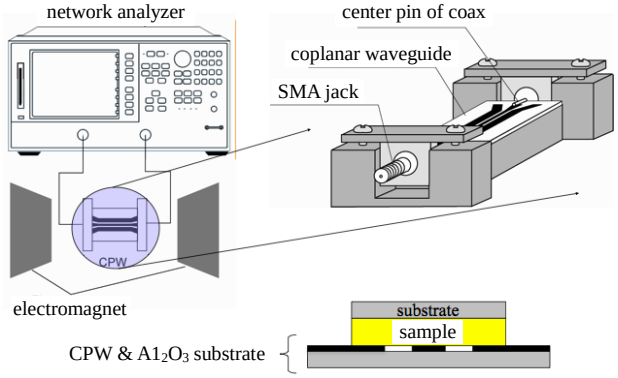

Fig. 3 The schematic of the flip-chip measurement set-up

4 Microwave assistant switching

4.1 Introduction

For an efficient magnetization switching it is very important to realize the magnetic motion that costs the lowest energy during its switching. The way of achieving the energetically efficient magnetization switching has been both theoretically and experimentally studied by using various adroit schemes[20-21]because it is one of the critical issues in the magnetic data storage applications where fast switching is essential for fast operation and low noise. In this section we investigate the possibility of using microwave to efficiently switch the magnetization. Furthermore, we will show that this technique may solve the issue of writing information on a high anisotropy K_u media which magnetic data storage industries are currently pursuing [12, 22].

The microwave assisted magnetization switching can also be derived from the LLG equation. In general, the motion of magnetization $\boldsymbol{M} = \boldsymbol{m}\, M_s$ under the influence of an effective magnetic field can be described by the normalized LLG equation[6-7]: $(1+\alpha^2)\mathrm{d}\boldsymbol{m}/\mathrm{d}t = -\boldsymbol{m}\times\boldsymbol{h}_t - \alpha\boldsymbol{m}\times(\boldsymbol{m}\times\boldsymbol{h}_t)$, where M_s is the saturation magnetization and α is a dimensionless damping constant. The total field, measured in unit of M_s, is written as a sum of an applied magnetic field $\boldsymbol{h}$ and the internal effective field $\boldsymbol{h}_i$ due to the magnetic anisotropy, i.e. $\boldsymbol{h}_t = \boldsymbol{h} + \boldsymbol{h}_i$. In the equation, time t is in a unit of M with the gyromagnetic ratio $(|\gamma|M_s)^{-1}$. From the LLG equation, the rate of energy change can be obtained [21]:

$$\frac{\mathrm{d}w}{\mathrm{d}t} = -\boldsymbol{m}\cdot\boldsymbol{h} - \frac{\alpha}{1+\alpha^2}|\boldsymbol{m}\times\boldsymbol{h}_t|^2 \qquad (16)$$

The second term on the right hand side is always negative, while the first term due to the external magnetic field can be either positive or negative if the field varies with time. Therefore, a time-dependent magnetic field can behave as an energy source and energy sink. When the magnetization gains energy from time-dependent magnetic field and overcomes the potential barrier between two states, the magnetization reverses its direction. This microwave assisted magnetization switching can be an efficient way to reverse magnetization since it can find a minimum energy path through the non-linear spin motion.

4.2 Experiments

We prepared magnetic tunneling junctions (MTJs) on top of a coplanar waveguide (CPW) by magnetron sputtering deposition, followed by conventional

photolithography and etching down process. The whole structure was prepared on Si (001) substrate with 1 μm thick SiO_2 layer. MTJs of Si/SiO_2/Cu (100 nm)/ $Ir_{24}Mn_{76}$ (15 nm)/$Fe_{30}Co_{70}$ (6 nm)/AlO_x (2.3 nm)/ $Ni_{80}Fe_{20}$ (20 nm)/Cu (70 nm) were fabricated on the signal line of the CPW so that microwave can be efficiently applied into the $Ni_{80}Fe_{20}$ layer shown in Fig. 4. The size of the MTJ is 50 μm ×70 μm . The magnetization in the $Fe_{30}Co_{70}$ bottom layer is fixed (no precession) by the $Ir_{24}Mn_{76}$ layer and the easy axis direction of $Ni_{80}Fe_{20}$ is made the same direction as the pinned direction. The CPW was designed to have 50 Ω impedance in absence of MTJ.

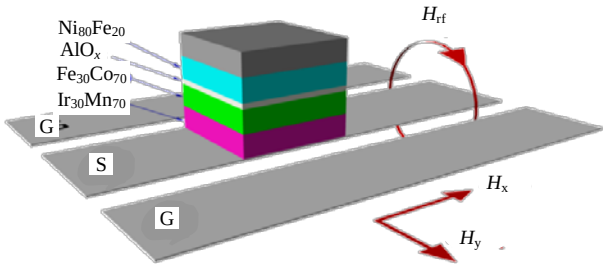

Fig. 4　Schematic illustration of a magnetic tunnel junction (MTJ) on a coplanar waveguide (CPW).

We introduced continuous microwave through the CPW and vary the input power from –2 dBm to 28 dBm and the frequency from 0.7 GHz to 4 GHz. The magnetic field component of microwave (H_{rf}) is linearly polarized and the direction is in the *y*-axis, as shown in Fig. 4. Microwave numerical simulation reveals that we have H_{rf} ~ 8.6 Oe at 1.5 GHz with 28 dBm input power. TMR was measured between top electrode of MTJ and the signal line in the presence of a microwave and an external dc magnetic field (H_{ex}). The measurement was performed at room temperature on a standard microwave probe station using lock-in technique to remove the noise. The schematic of the measurement setup is shown in Fig. 5. The CPW with a MTJ patterned on the signal line is placed between the Helmholtz coils. In order to remove the thermal effect on the switching due to microwave-induced heat, we conducted two different types of measurements. One is “hard-axis measurement” in which the $Fe_{30}Co_{70}$ moment (m_{FeCo}) and the external DC magnetic field (H_{ex}) direction are in the *x*-axis and H_{rf} is in the *y*-axis. The other is “easy-axis measurement” in which the m_{FeCo}, H_{ex}, and H_{rf} directions are all in the *y* direction. In the hard-axis measurement, H_{rf} is applied perpendicular to the magnetization and it exerts a torque to precess the spins. Thus, it is possible to induce a microwave-assisted magnetization switching in this geometry. On the other hand, in the easy axis measurement, there is no torque exerted on spin causing no spin precession because H_{rf} and spin are parallel to each other. Therefore, there is no possibility for microwave-assisted magnetization switching to occur in the easy-axis measurement, providing a reference measurement. The heat induced by microwave is same in both cases. By comparing these two measurements, we are able to eliminate the thermal effect and determine the microwave-assisted switching.

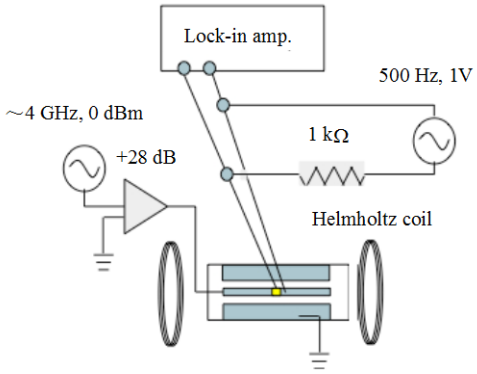

Fig. 5　Measurement set up for microwave assist magnetization switching.

Figure 6 shows magnetoresistance curves with three different microwave input powers at 1.5 GHz. The low and high resistance states indicate that magnetization of $Ni_{80}Fe_{20}$ is parallel and antiparallel to the $Fe_{30}Co_{70}$ magnetization.

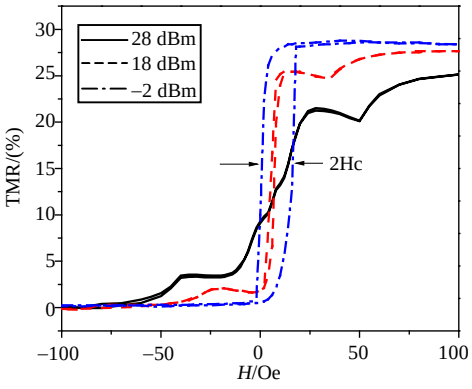

Fig. 6　Magnetoresistance curves with an application of 1.5 GHz microwave at 28 dBm, 18 dBm, and –2 dBm

We define the coercivity (H_c) as a half of the window width (Fig. 6). It is clear that the coercivity is reduced with increasing microwave power. At 28 dBm input power, the coercivity disappears completely. This leads to an under estimation of coercivity reduction at high power. The problem can be solved by using films of higher coercivity. Interestingly, besides the coercivity reduction, the saturation field increases and the remanence decreases with increasing the input power. The hysteresis loop becomes similar to a hard axis hysteresis loop. The slight asymmetry in the loops is due to a magnetic coupling with the $Fe_{30}Co_{70}$ bottom electrode, which is also observed in normal TMR measurement without microwave. The small dips above the saturation field, which can be also seen at other frequencies (Fig. 7a), are maybe related to a nonlinear FMR at 28 dBm and 18 dBm, which is both power and frequency dependent. These small dips are related to a nonlinear FMR with very large precession cone angle. We will discuss the nonlinear behavior of FMR in the following section. As we discussed previously, for the purpose of removing the thermal effect, we perform hard-axis and easy–axis measurements and results are shown in Fig. 7.

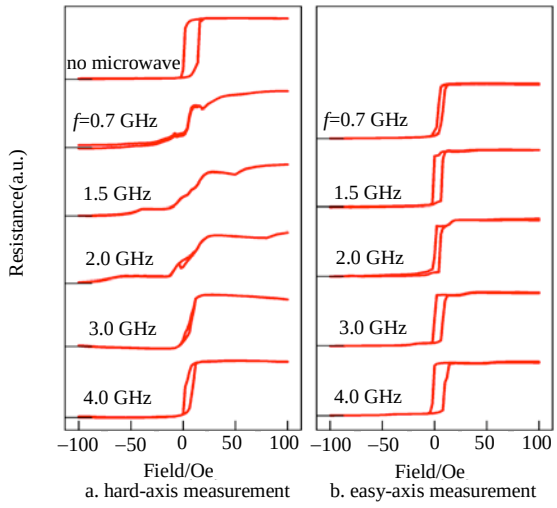

Fig. 7 Magnetoresistance curves in microwave with various frequencies from 0.7 GHz to 4 GHz at 28 dBm measured in different axis

In the easy-axis measurement, the loop shape is barely changed although there is a little coercivity reduction because of the thermal fluctuation. Furthermore, no dips at high dc magnetic field can be observed. On the other hand, in the hard-axis measurements, the hysteresis loops are dramatically changed in all the frequencies, although the coercivity reduction becomes smaller at higher frequencies. Moreover, the broad hysteresis shape is most pronounced in 1.5 GHz to 2 GHz range, which is corresponding to the natural resonance frequency (1.57 GHz) for the $Ni_{80}Fe_{20}$ layer estimated from flip-chip FMR measurement. This result is quite reasonable because spin precession toward the switching should be most pronounced at the natural resonance frequency. The probabilities of spin switching from 0° to180° and 180° to 0° are equal at H_{ex}=0, leading to zero magnetic remanence. As the field increases, one probability becomes larger than the other according to applied dc field direction, which broadens the hysteresis curves.

4.3 Discussion

We determine the coercivity reduction due to microwave by differencing the coercivity fields in easy-axis and hard-axis measurements at the same power and frequency. Fig. 8 shows the coercivity reduction as a function of microwave input power and frequency. The corresponding microwave field H_{rf} are estimated 8.6 Oe, 2.7 Oe, 0.86 Oe, and 0.27 Oe, respectively. Numerical simulation results are also plotted and areas under the curves are hatched for clarity. The corresponding uniaxial anisotropy k is also shown in the right axis.

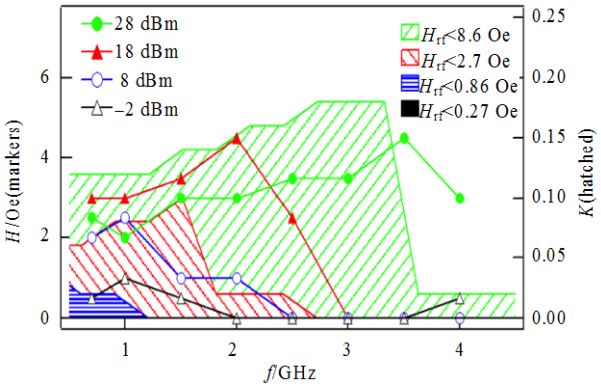

Fig. 8 Coercivity reduction as a function of frequency with microwave input power of 28 dBm, 18 dBm, 8 dBm,and –2 dBm

The coercivity reductions only at 28 dBm input power are under estimated since the coercivities have already been reduced to zero. As shown in Fig. 8a, the

microwave input power where maximum coercivity reduction occurs depends on the frequency and moves to higher power with increasing frequency. On the other hand, the input power also influences the frequency dependence of the coercivity reduction (Fig. 8b). The result implies that there is a mutual relation between microwave power and frequency for effective spin switching. To numerically simulate the power and frequency dependence of the coercivity reduction, we used the LLG equation and Eq. (16) with a normalized uniaxial magnetic anisotropy k described by $w(\boldsymbol{m},\boldsymbol{h}=0)=-km_x^2/2$ where $h_t=-\nabla_{\boldsymbol{m}}w(\boldsymbol{m},\boldsymbol{h}=0)$ [2]. In the calculation, we set k=1 corresponding to the anisotropy field H_k of $Ni_{80}Fe_{20}$. We used the parameters $\alpha=0.008$, $4\pi M_s$=10.8 kG, and H_k=30 Oe obtained from the flip-chip FMR measurement. Simulation results at different $H_{\rm rf}$ are plotted in Fig. 8b by hatching the areas under the curves for clarity. Although there is a mismatch between experimental and numerical simulation results, the trend of peak location depending on $H_{\rm rf}$ is correctly reproduced. Besides the data at 28 dBm input power, which is under estimated experimentally, numerical simulations seem to under estimate the experimental results. It should also be noted that the actual microwave power input to the sample might not be exactly constant throughout the frequencies because of the small frequency dependence of the CPW impendence. However, these small corrections are not expected to change the overall trend of our results.

5 Spin pumping

While conventional spin polarized transport properties have been understood, how precessing spins traverse through materials and interfaces still remains an interesting problem. In 1996, Slonczewski [8] and Berger[9] predicted that the spin current flowing through a magnetic multilayer could exert a spin-transfer torque on the magnetization, leading to magnetization precession and even reversal if the current density was large enough. Similarly, the precessing magnetizations in a ferromagnet excited by an RF external field can inject spins into neighboring layers, giving rise to the spin pumping effect [23-24]. There are two ways to detect spin pumping effect: 1) indirect measurement through Gilbert damping measurements, 2) direct measurement using electrical detection.

5.1 Indirect measurement of the spin pumping effect

Unlike the conventional spin-polarized current created by passing a current through a ferromagnet[25-29], the spin pumping effect utilizes an external microwave field to excite spin coherent precession at FM/NM interface. This coherent precession act as a "spin source", transferring angular momentum from the ferromagnet into the normal metal. A pure spin current is thus generated without any external voltage bias. In addition, the emitting spin current exerts a torque on the precessing spins, which effectively enhances the Gilbert damping in FM. In an adiabatic FM/NM system where the precession frequency of the magnetization is much smaller than the characteristic ferromagnetic exchange splitting, the total charge and spin current can be written as:

$$\begin{cases} I_c = I_c^{(0)} + I_c^{\rm pump} \\ I_s = I_s^{(0)} + I_s^{\rm pump} \end{cases} \tag{17}$$

where I_c and I_s are the total charge current and the total spin current, respectively. In the presence of the time-dependent spin precession, a spin current is pumped into the adjacent NM without a net charge current, thus:

$$\begin{cases} I_c^{\rm pump} = 0 \\ I_s^{\rm pump} = \dfrac{\hbar}{4\pi}\left(A_r^{\uparrow\downarrow} m \times \dfrac{{\rm d}m}{{\rm d}t} + A_i^{\uparrow\downarrow} \dfrac{{\rm d}m}{{\rm d}t} \right) \end{cases} \tag{18}$$

where $A^{\uparrow\downarrow}=A_r^{\uparrow\downarrow}+iA_i^{\uparrow\downarrow}=g^{\uparrow\downarrow}-t^{\uparrow\downarrow}$ is a device parameter that determines the magnitude of the spin pumping. It is a nonvanishing pumping parameter due to magnetism or any source of spin-dependent scattering. The quantities $t^{\uparrow\downarrow}$ and $t'^{\uparrow\downarrow}$ vanish when the FM layer is much thicker than the coherent length and the mixing conductance $g^{\uparrow\downarrow}$ and $g'^{\uparrow\downarrow}$ do not depend on the thickness of the FM[30]. The spin pumping current originates from the FM/NM interface. Spin pumping effect therefore is an interface effect and

is independent of the spin-flip process in the FM when it is far from the FM/NM interface on the scale of the spin diffusion length in the NM. However, a spin accumulation μ_s could be generated on the other side (NM) if the spin diffusion length of the NM is smaller than its thickness. This spin accumulation then induces a backflow spin current flowing toward the precessing ferromagnetic layer:

$$I_s^{\text{back}} = \frac{1}{4\pi}(A_r^{\uparrow\downarrow}\mu_s + A_i^{\uparrow\downarrow}\mu_s \times \boldsymbol{m}) \tag{19}$$

where μ_s is the spin accumulation build-up in the NM. The total spin current pumped into an adjacent NM layer by a precessing FM layer is:

$$I_s^{\text{pump}} = \frac{\hbar}{4\pi}(\text{Re}\, A_{\text{eff}}^{\uparrow\downarrow}\boldsymbol{m} \times \frac{\text{d}\boldsymbol{m}}{\text{d}t} + \text{Im}\, A_{\text{eff}}^{\uparrow\downarrow}\frac{\text{d}\boldsymbol{m}}{\text{d}t}) \tag{20}$$

where m is the unit vector along the instantaneous direction of the precessing magnetization and $A_{\text{eff}}^{\uparrow\downarrow}$ is the effective spin pumping efficiency (in units of $\frac{e^2}{\hbar}$).

Similar to spin transfer torque, the spin current due to the spin pumping effect generates additional torque τ on precessing magnetizations in FM. This torque drives the transverse magnetization. The component parallel to m does not contribute and can be projected as $\tau = -m \times I_s \times m$. Therefore, the torque can be written as an additional term in the LLG equation as:

$$\frac{\partial m}{\partial} = \frac{\gamma}{M_s V}\boldsymbol{m} \times I_s \times \boldsymbol{m} \tag{21}$$

where M_s is the saturation magnetization and V is the volume of the ferromagnet. This torque acts as a friction force on the precessing spins and induces the enhancement of the Gilbert damping constant in FM. As shown in Eq. (20), this torque depends on $A_{\text{eff}}^{\uparrow\downarrow}$, an interface property of F/N and the spin relaxation property in NM as well. The effective spin pumping efficiencies $A_{\text{eff}}^{\uparrow\downarrow}$ can be written as [24]:

$$\frac{1}{A_{\text{eff}}^{\uparrow\downarrow}} = \frac{1}{g^{\uparrow\downarrow}} + \frac{R_{\text{sd}}}{\tanh(L/\lambda_{\text{sd}})} \tag{22}$$

where $g^{\uparrow\downarrow}$ is the spin mixing conductance at the F/N interface, R_{sd} is the dimensionless resistance (in units of $\hbar/2e^2$) of the NM layer with the thickness L, and the spin diffusion length in NM λ_{sd}. Therefore, the effective Gilbert damping constant is

$$G_{\text{eff}} - G = \left[1 + g^{\uparrow\downarrow}\frac{R_{\text{sd}}}{\tanh(L/\lambda_{\text{sd}})}\right]\frac{\hbar\gamma 2 g^{\uparrow\downarrow}}{4\pi V} \tag{23}$$

The prefactor on the right-hand side of Eq. (23) indicates the reduction effect on the Gilbert damping is caused by the back flow spin current. Thus the enhancement of effective Gilbert damping depends on the material of the NM layer that has a different $g^{\uparrow\downarrow}$ and a spin diffusion property λ_{sd}. For example, Pt and Cu both have similar $g^{\uparrow\downarrow}$. While Pt has a relatively short λ_{sd} which gives a large enhancement of effective Gilbert damping, Cu provides little to no enhancement due to its long λ_{sd}.

5.1.1 Gilbert damping in spin valves (SVs)

In ferromagnet/normal metal/ferromagnet (F_1/N/F_2) double layer structures where F_1 is precessing, the second ferromagnet F_2 acts as a spin sink for the spin current pumped by the first ferromagnet. If F_2 is also precessing, mutual pumping could exit. The mutual exchange of spin currents between F_1 and F_2 leads to a dynamic exchange coupling that is almost independent of thickness of the spacer layer, if it does not exceed the spin diffusion length, in contrast to static interlayer exchange coupling. Ignoring the static exchange interaction between F_1 and F_2, the new effective spin pumping efficiency $A_{\text{F}_1/\text{N}/\text{F}_2}^{\uparrow\downarrow}$ can be written as:

$$\frac{1}{A_{\text{F}_1/\text{N}/\text{F}_2}^{\uparrow\downarrow}} = \frac{1}{g_1^{\uparrow\downarrow}} + \frac{2e^2}{h}\frac{L}{S\sigma} + \frac{1}{g_2^{\uparrow\downarrow}} \tag{24}$$

where σ is the conductivity of the NM layer with thickness L and lateral section area S. For small angle precession, the magnetization dynamics in the presence of dynamic exchange coupling can be described with a modified LLG equation

$$\frac{\text{d}m_i}{\text{d}t} = -\gamma \boldsymbol{m}_i \times H_{\text{eff}}^i + \alpha_i^{(0)}\boldsymbol{m}_i \times \frac{\text{d}m}{\text{d}t} + \alpha_i\left(\boldsymbol{m}_i \times \frac{\text{d}\boldsymbol{m}_i}{\text{d}t} - \boldsymbol{m}_j \times \frac{\text{d}\boldsymbol{m}_j}{\text{d}t}\right) \tag{25}$$

where $m_{i,(j)}$ are the unit vectors along the instantaneous magnetization direction in F_1 and F_2 layers, respectively. $\alpha_i^{(0)} = \frac{G_i}{\gamma_i G_{i,s}}$ is the intrinsic damping constant and $\alpha_i' = \frac{G_i'}{\gamma_i G_{i,s}}$ is the additional damping

contribution from the spin pumping and sink effects, where $G_i' = \frac{\hbar\gamma_i^2 A_{F_i/N/F_2}^{\uparrow\downarrow}}{4\pi d_i S}$ with thickness d_i of F_i and lateral area S. The net spin current generated by the spin pumping of F_1 layer propagates away from the F_1/N interface and is absorbed at the N/ F_2 interface if N is thinner than the spin diffusion length. Conservation of angular momentum requires that layer F_1 loses spin momentum, which leads to an increase of the Gilbert damping parameter for F_1 layer. If the magnetization in F_2 is static, the effective Gilbert damping will be $G_{\text{eff}} = G^{(0)} + G^{\text{n}}$ because the m_2 term in Eq. (18) vanishes. Up to now, several groups have studied the Gilbert damping in the F_1/N/ F_2 multilayer[31-33], where the magnetization of F_1 is precessing and that F_2 is either precessing or static. In a recent work, Heinrich et al. studied the magnetization relaxation in GaAs(001)/Fe/Au/Fe/Au multilayers [32]. They observed a sudden narrowing of the FMR linewidth when both FMs reach the identical resonance and their magnetizations were in parallel configuration. Under this condition, the dynamic coupling quickly synchronizes its motion and equalizes the spin currents. Since the spin currents from both FM layers are canceled out, there is no additional contribution to Gilbert damping. The Gilbert damping in this layered system is the same as in the bulk Fe. In this work, we studied the magnetization dynamics in the IrMn/FeCo/Cu/NiFe/Cu spin valve. The NiFe is the free layer (precessing layer) and the FeCo layer is magnetically pinned by IrMn, which enables us to study the magnetization dynamics not only in parallel, but also antiparallel configurations between the magnetizations of the NiFe and FeCo layers. Furthermore, different FM layers allow us to separate the FMR fields and have better control of the static and precessing states of FeCo magnetization. Our results show that the Gilbert damping constant of NiFe is enhanced in antiparallel configuration when the magnetizations of both FM layers are precessing.

The sample structure is composed of Si(001)/SiO_2 (1 μm)/ Cu (100 nm)/IrMn (15 nm)/FeCo (6 nm)/Cu (10 nm)/ NiFe (8 nm)/Cu (70 nm)/Au (30 nm), fabricated by magnetron sputtering deposition. The magnetic property is shown in Fig. 9b where the hysteresis loop is measured by a VSM. As shown in Fig.9, the pining field on the bottom FeCo layer is about 150 Oe, which leads to a well separated parallel and antiparallel magnetization configurations. Typical normalized $\chi''(H)$ spectra at 2.1 GHz and 3.3 GHz are shown in Fig. 9a.

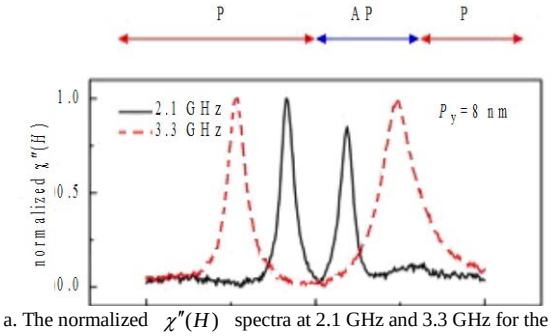

a. The normalized $\chi''(H)$ spectra at 2.1 GHz and 3.3 GHz for the spin valve with Cu spacer layer

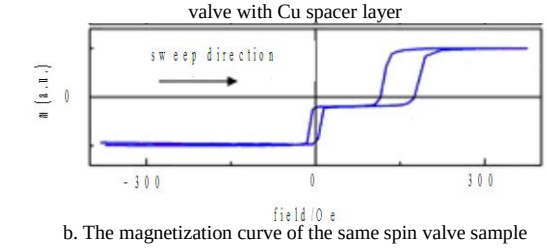

b. The magnetization curve of the same spin valve sample

Fig. 9 The magnetic behavior of the spin valve sample

Our previous experiment results[34] showed that the Gilbert damping constant of the NiFe layer is enhanced at an AP state compared to P state. However, the source of the enhancement has yet to be experimentally confirmed. In Fig. 9a, the FMR peaks in the negative (positive) field correspond to parallel (antiparallel) magnetization states. While the linewidth of the peak is obviously broader in the AP state than P state at 3.3 GHz, the same does not supply at 2.1 GHz where the linewidths of the peak at both AP and P states are similar. Comparing FMR spectra and the hysteresis loop, the FMR field of the AP state at 2.1 GHz is well within the defined antiparallel state with no magnetization switching. This is not the case at 3.3 GHz. The field overlapping between FMR peak and FeCo loop at 3.3 GHz suggests that the magnetization of FeCo is not rigidly fixed and may begin to precess under the same microwave excitation. The results in Fig. 9 suggest that the enhancement of the Gilbert damping constant (directly proportional to the linewidth of FMR peak) occurs when the magnetization configuration is at AP state and the magnetizations of both FM layers are precessing.

Fig. 10 shows the FMR frequency in the IrMn/FeCo/Cu/NiFe/Cu spin valve as a function of the magnetic field applied along the opposite direction of the FeCo pinning field. The circle and triangle symbols represent the experimental data for the NiFe layer and the FeCo layer, respectively. The solid lines are the fitting results. The plots are well fitted by Kittel model for thin films. The extracted parameters $4\pi M_s = 8970$G, $H_k = 12$ Oe for the NiFe layer and $4\pi M_s = 18800$G, $H_k = 88$ Oe for FeCo layer are quite reasonable and consistent with the magnetization curves shown in Fig. 9b. Here, H_k is the effective anisotropy field. As shown in Fig. 10, in the negative field, the FMR frequencies for NiFe and FeCo are well separated, and only NiFe is precessing in our experimental conditions. There are two regions with AP configuration in the positive field 0 Oe to 300 Oe . From 0 Oe to 150 Oe(dark area), the FMR of NiFe and FeCo are reasonably separated and only NiFe can be precessed with stationary FeCo magnetization. From 150 Oe to 300 Oe(light area) FeCo and Py resonant frequencies overlap between 2.5/GHz to 3.3 GHz. At these resonant frequencies and fields, the magnetizations in both FeCo and Py layers precess. Therefore both FMs act as spin pumping and sinking sources.

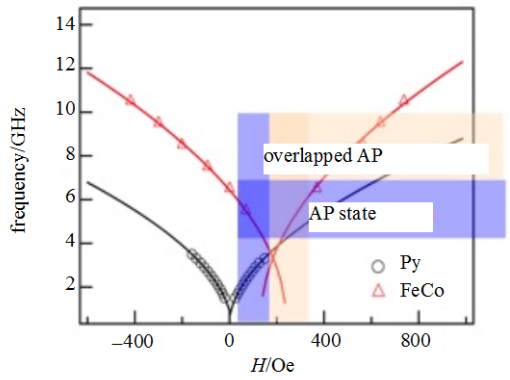

Fig. 10 The FMR frequency in the IrMn/FeCo/Cu/NiFe/Cu spin valve as a function of the magnetic field applied along the opposite direction of the FeCo pinning field

The linewidth of FMR peaks at different frequencies are extracted from the FMR spectra. Fig. 11 shows the linewidth ΔH of NiFe as a function of the frequency in the IrMn/FeCo/Cu/ NiFe/Cu spin valve. The square symbols are for the parallel state, and the circle and triangle symbols are for the antiparallel state but in non-overlapping and overlapping regions, respectively. The Gilbert damping constants corresponding to different states and regions are extracted using the fitting. dH increases linearly as frequency increases in the P state. The extracted effective Gilbert damping constant is $G_{\text{eff}} = 0.832\times10^{-8}$ S^{-1}. dH in the AP state has a discontinuity in its slope when the field is increased from the non-overlapping region to overlapping region. The extracted Gilbert damping constants are $G_{\text{eff}} = 1.003\times10^{-8}$ S^{-1} in the non-overlapping region and $G_{\text{eff}} = 3.769\times10^{-8}$ S^{-1} in the overlapping region. The latter is more than four times larger compared to the Gilbert damping constant in the P state.

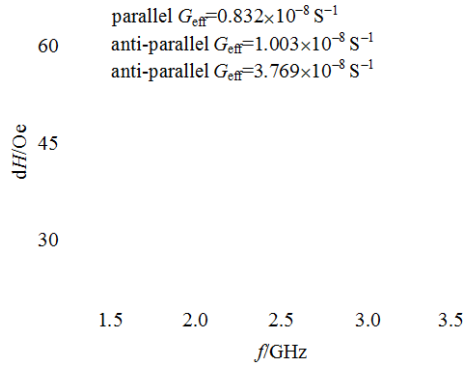

Fig. 11 The linewidth ΔH of NiFe as a function of the frequency in IrMn /FeCo /Cu /NiFe /Cu spin valves.

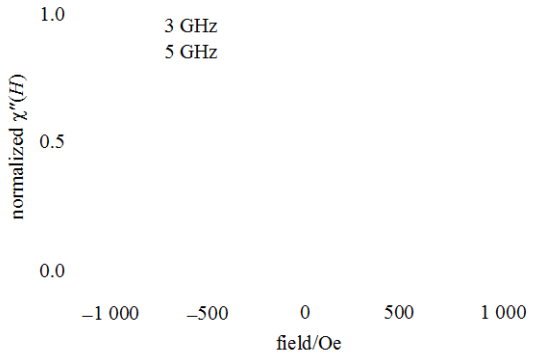

Fig. 12 The normalized $\chi''(H)$ spectra at 3 GHz and 5 GHz for the spin valve with a Cu spacer layer

This result indicates that the AP state and the precessing magnetizations of both FM layers are required to induce the enhancement of the Gilbert damping constant compared to the P state. The AP state itself does not necessarily enhance the damping. It

suggests that the dynamic exchange between NiFe and FeCo may be the main mechanism that induces the Gilbert damping enhancement in NiFe layer through the pumping and sinking effects.

Before making the final conclusion that the dynamic exchange is the main mechanism of the enhanced Gilbert damping constant in AP state, there is another possible mechanism we have to consider: two overlapping FMR peaks could broaden dH. Theoretically, this is possible when two FMR peaks are close enough and the FMR measurement is only based on the microwave absorption in the sample. Therefore, we carefully examined this possibility in the experiments. When two FMR peaks overlap with each other, the maximum peak magnitude of the overall peak must be larger than each single peak. This is clearly shown at the 5 GHz $\chi''(H)$ spectrum in Fig. 12. The peak at the positive field that consists of both NiFe and FeCo peaks is obviously higher than the one at the negative field where only the single NiFe peak exists. However, this scenario does not appear at the 3 GHz spectrum, where we observed the enhancement of the Gilbert damping constant. Therefore, this indicates that the overlapping FMR peaks are not responsible for the enhancement in our experiments.

The final conclusion can be made now based on the experiment results above and the discussions. We believe the dynamic exchange between two FM layers induces the Gilbert damping enhancement in the IrMn/FeCo/Cu/NiFe/Cu spin valve. The experiment results can be explained well under the dynamic exchange theory. Assuming the magnetizations of both NiFe and FeCo are precessing at the same frequency, we can write:

$$\frac{\mathrm{d}\boldsymbol{m}_1}{\mathrm{d}t}=\frac{\mathrm{d}\boldsymbol{m}_2}{\mathrm{d}t} \tag{26}$$

where subscripts 1 and 2 represent NiFe and FeCo layers respectively. Therefore, the Eq. (25) can be rewritten as:

$$\frac{\mathrm{d}\boldsymbol{m}_1}{\mathrm{d}t}=-\gamma\boldsymbol{m}_1\times H_{\mathrm{eff}}^1+\alpha_1^{\mathrm{eff}}\boldsymbol{m}_1\times\frac{\mathrm{d}\boldsymbol{m}_1}{\mathrm{d}t} \tag{27}$$

where the effective damping constant is:

$$\alpha_1^{\mathrm{eff}}=\alpha_1^{(0)}+\alpha_1'\frac{(\boldsymbol{m}_1-\boldsymbol{m}_2)}{\boldsymbol{m}_1}=\frac{G_1^{\mathrm{eff}}}{\gamma M_{1,s}} \tag{28}$$

where the first term on the right hand is the normal damping constant and the second term represents the additional damping induced by spin pumping and sinking effects.

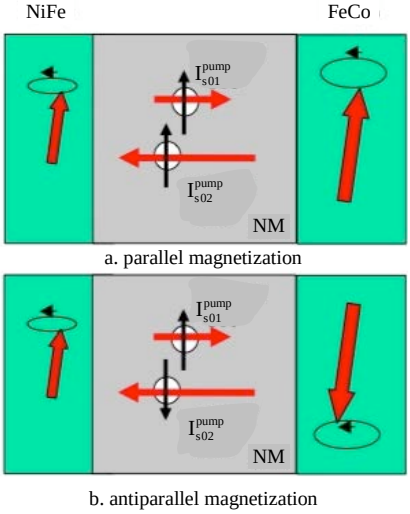

Fig. 13　The schematic picture of the dynamic exchange between NiFe and FeCo layers in spin valves with two different magnetization configurations

For the parallel state, $G_1^{\mathrm{eff}}\leqslant G_1^{(0)}$ because $\boldsymbol{m}_1\leqslant\boldsymbol{m}_2$ and the second term in Eq. (28) becomes either negative or zero. This is consistent with the sudden decrease of dH found in Heinrich's observation in the GaAs(001)/Fe/Au/Fe/Au spin valve [32]. However, for the antiparallel state, the effective Gilbert damping constant becomes $G_1^{\mathrm{eff}}=G_1^{(0)}+\frac{(\boldsymbol{m}_1+\boldsymbol{m}_2)}{\boldsymbol{m}_1}G_1'\geqslant G_1^{(0)}+2G_1'$ since m_2 is in the opposite direction of m_1. Therefore, the Gilbert damping is enhanced through the dynamic exchange. The schematic picture of the dynamic exchange in spin valves is shown in Fig. 13 for parallel and antiparallel configurations.

To briefly conclude this section, we have experimentally studied the magnetization dynamic in an IrMn/FeCo/Cu/NiFe/Cu spin valve through the Gilbert damping. Our results show that the Gilbert damping constant of NiFe is enhanced in an antiparallel configuration when the magnetizations of both FM layers are precessing. This enhancement is induced by the dynamic exchange between the magnetizations of NiFe and FeCo layers. We are also able to qualitatively explain the spin dependent Gilbert

damping enhancement with a simple dynamic exchange model based on spin pumping.

5.1.2 Gilbert damping in magnetic tunneling Junctions (MTJs)

We have also experimentally investigated the Gilbert damping of $Ni_{80}Fe_{20}$ in Cu/IrMn/$Fe_{30}Co_{70}$ / AlO_x/ $Ni_{80}Fe_{20}$/Cu MTJs in parallel and antiparallel magnetization configurations by a flip-chip FMR measurement with a coplanar waveguide (CPW). The Gilbert damping constant was estimated from the FMR linewidth. MTJ structures Cu (100 nm)/IrMn (15 nm)/ $Fe_{30}Co_{70}$ (6 nm)/AlO_x (2.3 nm)/$Ni_{80}Fe_{20}$ (d_{NiFe} nm)/Cu (70 nm) were fabricated on Si (001) wafer with 1 μm thermal oxide layer by magnetron sputtering deposition under the base pressure 10^{-8} Torr. The bottom $Fe_{30}Co_{70}$ electrode is magnetically pinned by IrMn. The aluminum oxide barrier was formed by plasma oxidation following the Al deposition. The oxidation of the barrier was optimized by using a wedge-shaped layer technique. The tunneling magnetoresistance (TMR) and the resistance area product were measured to be 29% and $1.3\times10^5\Omega\cdot m^2$, respectively.

Fig. 14 shows the thickness dependence of the effective Gilbert damping constant for three structures in which two ferromagnets NiFe and FeCo are separated by different spacers. For the structure with AlO_x spacer, we find that in the P state G_{eff} is almost independent of the $Ni_{80}Fe_{20}$ thickness, whereas the strong thickness dependence is observed in the AP state. The nearly linear dependence on the $1/d_{NiFe}$ in the AP state indicates that G_{eff} enhancement may originate from the surface (interface) effects, similarly to the explanation of Gilbert damping enhancement experiments on FM/NM multilayers in terms of the spin pumping theory. However, the conventional spin pumping theory [24] predicts a negligible spin pumping through a tunnel barrier, and, therefore, no damping enhancement in MTJ structures. In another words, only G_{eff} behavior in P state is consistent with conventional spin pumping theory.

Our exploration of magnetization dynamics effects in tunnel structures indicate that, direct spin pumping through a barrier does exist. The dynamics of the magnetization in one ferromagnet can be influenced by the second ferromagnet through the spin pumping. Thus, the damping enhancement observed in AP state here could have a similar origin as the one in SV structure we discussed in the previous section. We stress that the Gilbert damping enhancement at AP state disappears in very thick barriers, which is reasonable considering the thick barrier suppresses the tunneling current.

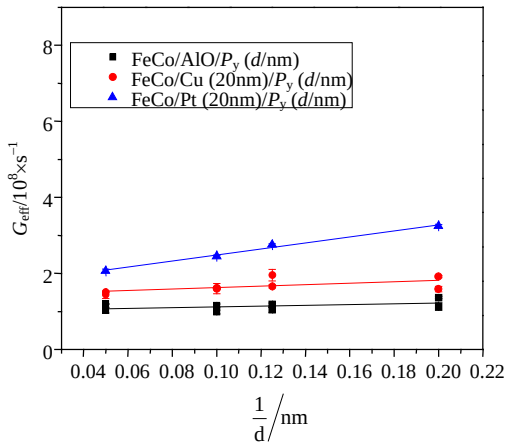

b. parallel configuration

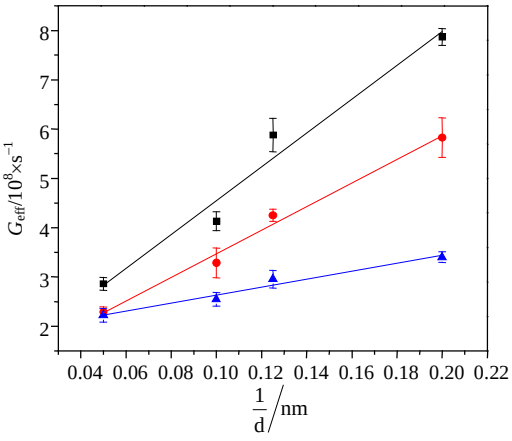

a. antiparallel configuration

Fig.14 The effective Gilbert damping constant as a function of the inversed thickness of NiFe layer. The spacer between two ferromagnets is AlO_x (circle symbols), Cu (square symbols), and Pt (triangle symbols) respectively

5.2 Direct measurement of spin pumping effect

5.2.1 Spin Valves

The spin injection into a nonmagnetic layer gives rise to a spin accumulation via chemical potential splitting between spin-up and spin-down electronic bands. A second ferromagnetic layer via a tunneling barrier can be used to detect this splitting. The observed voltages are expected to vary depending on the relative orientation between the magnetization of

the detecting ferromagnet and the net moment direction in the normal metal. The largest voltage difference $p\mu_s$ should be observed between parallel and antiparallel states, where $p=(G_\uparrow-G_\downarrow)/(G_\uparrow+G_\downarrow)$ is the relative polarization of the spin-dependent tunnel conductance G of the detector and μ_s is the spin accumulation in the normal metal [24] written as:

$$\mu_s=\hbar\omega\frac{\sin^2\theta}{\sin^2\theta+\eta} \tag{29}$$

where $\eta=\tau_i/\tau_{sf}$ is a reduction factor expressed in the ratio between the spin-flip rate and the spin injection rate, defined as theta. In a recent letter, Wang proposed a simple scheme to electrically measure the spin accumulation[35]: A F/N layer is used to convert pumped spin accumulation into a charge voltage. The single ferromagnet serves as both the source and detector for spin pumping current. The detection is realized by partially absorbing the back flow spin current through spin flip scattering, thus generating a net charge voltage caused by the spin dependent interface and bulk conductance. Under the assumption that the thickness of the N layer is much smaller than its spin diffusion length, the voltage across the FM/NM interface is:

$$V_{dc}=\frac{p_\omega g_F\sin^2\theta\cos\theta}{(g_\omega-p_\omega^2 g_\omega+g_F)(\eta_N+\sin^2\theta)+(1-p_\omega^2)g_F\cos} \tag{30}$$

where $\eta_N=g_N/g_\omega^{\uparrow\downarrow}\tanh(d_N/\lambda_{sd}^N)$ is a reduction factor with the thickness d_N and the spin diffusion length λ_{sd}^N of a normal metal layer, and g_F and g_N are the bulk conductance of FM and NM layers, respectively. $g_\omega=g_\omega^\uparrow+g_\omega^\downarrow$ is the sum of the spin-up and spin-down effective conductances at the FM/NM interface. $g_\omega^{\uparrow\downarrow}$ is the real part of the effective spin-mixing conductance; p_ω is the interfacial spin polarization. Based on this scheme, a direct electrical detection of the spin pumping effect has been realized recently in an N/F/N trilayer [36]. The voltage signals of the order of 100 μV were observed, which is in good agreement with the theory.

5.2.2　F/I/N Structure

Unlike the spin-transfer torque where electrons are forced through the tunneling barrier, the spin pumping effect is not expected in tunneling structures because the spin injection rate is negligibly smaller than the spin relaxation rate. Nevertheless, our recent experiment[37] has indicated that more subtle physics concerning the spin and charge pumping occur in tunneling structures, which appear to be very different from N/F/N structures.

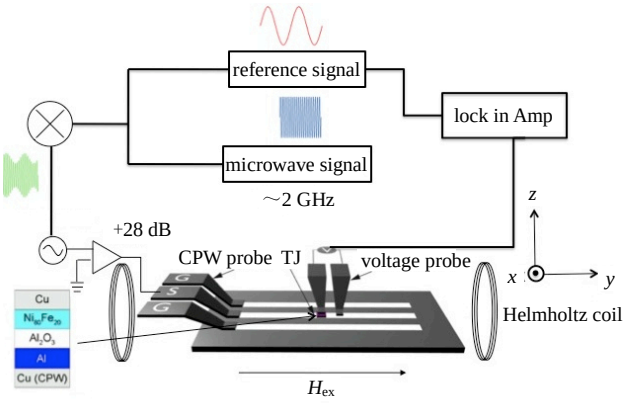

Fig. 15　Schematic diagram of the sample geometry and the experimental setup.

In an experiment involving a nanometer thick tunneling junction structure and microwaves, how efficient microwave power can be coupled into the tunneling junction becomes a challenge. We chose a coplanar waveguide (CPW) to solve this problem because the planar structure would be advantageous in terms of device integration for possible spin pumping applications and the dimension of CPW also fits tunneling junctions. The sample geometry and the experiment setup are illustrated in Fig. 15. The modulated microwave signal is fed into the coplanar waveguide through an FPC probe. The tunneling junction is on the top of the signal line and the dc voltage generated across the tunneling junction is measured using a lock-in technique.

The tunneling junction was directly fabricated on the top of the CPW signal line. The underlying CPW of 50 Ω characteristic impedance was also designed to avoid the impedance mismatch with the RF probes. The tunneling junction structure is composed of Si/SiO_2/Cu (100 nm)/Al (10 nm)/AlO_x (2.3 nm)/$Ni_{80}Fe_{20}$ (20 nm)/Cu (70 nm)/Au (25 nm). It was fabricated using magnetron sputtering deposition and the AlO_x tunnel barrier was formed by in-situ plasma oxidation. After the deposition, two steps of microfabrication were performed. The CPW structures made from the bottom 100 nm Cu layer were formed at the first step and the tunneling junction pillars with the size of 50 μm × 50 μm were fabricated on top of the

center CPW signal line after the second step. The resistance of the tunneling junction pillar was about 67 kΩ. A microwave signal from an Agilent 8753B vector network analyzer was fed into the CPW and generated a microwave magnetic field H_{rf} along the *x*-axis in the plane of the tunneling junction. A Helmholtz coil was used to apply a dc magnetic field up to 120 Oe along the CPW (*y*-axis). The magnetization thus mainly precessed along the *y*-axis. The voltage across the tunneling junction was measured by contacting a Cascade FPC probe on top of the tunneling junction to the CPW signal line. The microwave frequency varies from 0.7 GHz to 4 GHz with power up to 25 dBm. The microwave amplitude was modulated with a sinusoidal signal of several hundreds hertz provided by a function generator in order to allow the use of the lock-in detection technique. One factor we must point out is the inevitable existence of a few tens of microvolt background voltage in the experiments, even without an applied magnetic field. This dc background voltage is probably due to the rectification effect that we will discuss later in this chapter. We found that the background voltage was directly proportional to the input microwave power. The larger the power is, the bigger the background voltage is. By slightly tuning the nominal input power (±1 dBm), the same power applied to the device can be achieved at different frequencies, which gives the same background voltage within 20% error. Therefore, the data between different frequencies can be compared without concerning the frequency dependence of the CPW impedance.

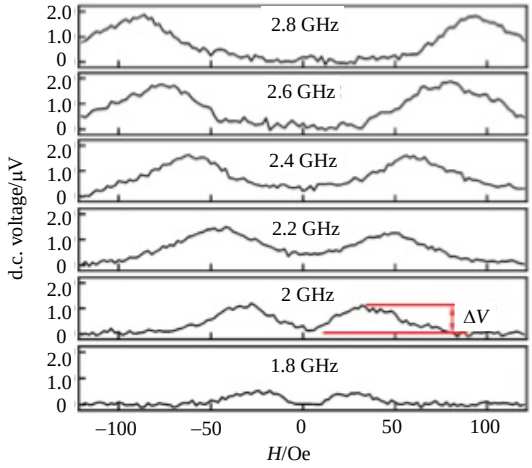

a. The dc voltage generated across the Al/AlO$_x$/Ni$_{80}$Fe$_{20}$/Cu tunneling junction as a function of the external static magnetic field

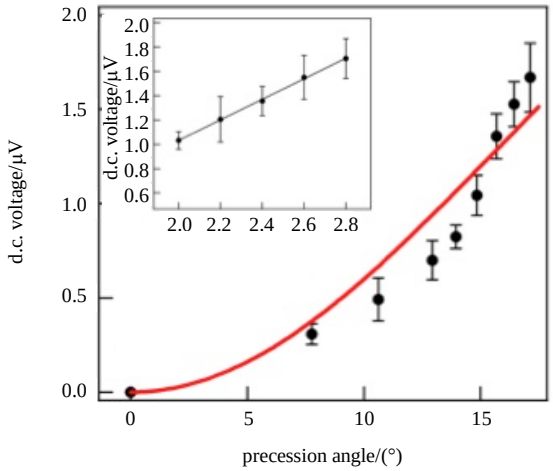

b. The dc voltage Δ*V* as a function of the precession angle with the solid line being the fitting. The inset in (b) shows the voltage as a function of the frequency at 10 dBm microwave power

Fig. 16 The DC voltage charateresties of the AL/ALO$_x$/Ni$_{80}$Fe$_{20}$/Cu tunheling junctio

Fig. 16a shows the measured dc voltage as a function of the external static magnetic field for an Al/AlO$_x$/Ni$_{80}$Fe$_{20}$/Cu tunneling junction. The frequency of the microwave field varies from 1.8 GHz to 2.8 GHz. The symmetrical peaks appears at both positive and negative fields at all microwave frequencies and the magnitude of the peaks is of the order of μV, one order larger than the reported values for an N/F/N structure[36]. The peak position as a function of the microwave frequency can be well fitted by the Kittel formula yielding parameters consistent with those of Ni$_{80}$Fe$_{20}$. This result indicates the voltage peaks are strongly correlated to the FMR of the Ni$_{80}$Fe$_{20}$ layer [6].

The frequency and the precession angle dependence of the dc voltage are shown in Fig. 16b. The linear relation between Δ*V* and the frequency is evident. The precession angle θ under the microwave excitation is estimated from $\Delta R/R \propto (1-\cos\theta)$ where the TMR changes were measured in IrMn/Fe$_{70}$Co$_{30}$/AlO$_x$/Ni$_{80}$Fe$_{20}$ MTJ under an electrical bias of 20 mV. Although the voltage signal is clearly from FMR excitation in the Ni$_{80}$Fe$_{20}$ layer, other possible sources like the electrical rectification effect must be eliminated before a qualitative description can be given. The simple structure of the F/I/N tunneling junction makes it naturally immune to the TMR rectification

effect since there is only one single ferromagnet. Although the time dependent anisotropy magnetoresistance (AMR) and the anomalous Hall effect (AHE) could exist, the analysis of our measurement geometry indicates that no dc voltage component could be generated across the junction by those two effects [6]. Thus, no dc voltage generated due to the rectification effect is expected in our tunneling junction under designed measurement geometry. Further investigation in Al/$Ni_{80}Fe_{20}$/Cu and Cu/AlO_x/Al/$Ni_{80}Fe_{20}$/Cu structures also supports that the voltage across the Al/AlO_x/$Ni_{80}Fe_{20}$/Cu tunneling junction was indeed from the AlO_x/$Ni_{80}Fe_{20}$ interface.

At the first glance, the results in Fig. 16b can be well fitted with Eq. (30). However, the extracted parameters are not physically reasonable. The linear fitting of ΔV versus the frequency in the inset of Fig. 16b gives rise to $g_\omega^{\uparrow\downarrow}/g_\omega \approx 6.1$ at a precession angle of 17°, which is too large compared to the estimated value of 0.5 for tunneling contacts[38]. While $\eta_N \approx 0$ is required to fit our precession angle dependence data, this is impossible in a tunneling junction, considering the conductance of a nonmagnetic layer g_N should be several orders of magnitude larger than the effective spin-mixing conductance $g_\omega^{\uparrow\downarrow}$ at F/I interface. All these discrepancies originated from the fact that the standard spin pumping theory is developed to treat multilayer of ohmic interfaces. From this theory, the spin pumping effect is never expected in a tunneling junction structure where the conductance mismatch at the F/I interface impedes the charge current flowing, thus destroying the pumped spin current. Our results suggest more complex physics exist in the tunneling junction structure. One possible mechanism is the spin charge coupling at the F/I interface[39]. A large voltage in the order of 1~100 μV is predicted by considering the electron-electron interaction, because of the huge difference of the scales associated with the charge screening length ($\approx 10^{-10}$ m) and with the spin diffusion length ($\approx 10^{-8}$ m).

To conclude this section, we have experimentally observed the dc voltage generation across the tunneling barrier while the spin precession is excited in the ferromagnetic free layer by the microwave field. The magnitude of the dc voltage peak is around a few μV with an AlO_x tunneling barrier, which is about an order larger than the signal obtained in an N/F/N structure [36]. These results cannot be explained by the conventional spin pumping theory[24] because it only deals with Ohmic F/N interfaces. The spin pumping effect is never expected in a tunneling junction structure where the conductance mismatch at the F/I interface destroys the pumped spin current. Our results directly indicate that spin current can be pumped through the tunneling barrier, thus generating the dc voltage across the barrier. More detailed experiments and theory studies are certainly needed in order to fully understand the role of the F/I barrier interface in the spin pumping mechanism. The devices represent a passive microwave detector.

6 Concluding remarks

Microwave experiments with spintronic devices have been presented here. Two spin dynamic properties, microwave assistant switching and spin pumping effect, have also been presented. Spintronic devices are intrinsically non-linear devices, similar to conventional RF diodes which are used to detect microwave power. There is no question that microwave devices based on spintronic devices will surface. They can be used as microwave detectors, capable of detecting microwave power, frequency, and phase. Furthermore, modulation and demodulation can also been implemented. With spin torque oscillator being demonstrated, these miniaturized spintronic devices, with lateral dimension of nanometer scale, have huge potential for chip-level microwave communication, network analyzer on a chip, and microwave image.

References

[1] MOTT N F. The resistance and thermoelectric properties of the transition metals[C]//Proceedings of the Royal Society of London. London: Royal Society of London, 1936: 368-382.

[2] O'HANDLEY R C. modern magnetic materials: Principles and applications[M]. New York: John Wiley & Sons, Inc.,

2000.

[3] JULLIERE M. Tunneling between ferromagnetic Films[J]. Physics Letter A, 1975 54A: 225-226.

[4] MIYAZAKI T, TEZUKA N. Giant magnetic tunneling effect in Fe/Al_2O_3/Fe junction[J]. J Magn Magn Mater, 1995,139(3): L231-234 .

[5] MOODERA J S, KINDER L R, WONG T M, et al. Large magnetoresistance at toom temperature in ferromagnetic thin film tunnel junctions[J]. Physical Review Letters, 1995, 74(16): 3273-3276 .

[6] BUTLER W H, ZHANG X G, Schulthess T C, et al. Spin-dependent tunneling conductance of Fe|MgO|Fe sandwiches[J]. Phys Rev B, 2001, 63(5): 054416.

[7] MATHON J, UMERSKI A, Theory of tunneling magnetoresistance of an epitaxial Fe/MgO/Fe(001) junction[J]. Phys Rev B, 2001, 63(22): 220403.

[8] SLONCZEWSKI J C. Current-driven excitation of magnetic multilayers[J]. J Magn. Magn Mater, 1996, 159: L1-L17.

[9] BERGER L. Emission of spin waves by a magnetic multilayer traversed by a current[J]. Phys Rev B, 1996, 54: 9353-9358 .

[10] HANKIEWICZ E M, Vignale G, TSERKOVNYAK Y. Inhomogeneous Gilbert damping from impurities and electron-electron interactions[J]. Phy Rev B, 2008, 78: 020404(R).

[11] KHITUN A, NIKONOV D E, BAO M. Feasibility study of logic circuits with a spin wave bus[J] Nanotechnology, 2007, 18: 465202.

[12] MORIYAMA T, CAO R, XIAO Q, et al, Microwave-assisted magnetization switching of $Ni_{80}Fe_{20}$ in magnetic tunnel junctions[J]. Appl Phys Lett, 2007, 90: 152503 .

[13] KISELEV S I, SANKEY J C, KRIVOROTOV I N, et al., Microwave oscillations of a nanomagnet driven by a spin-polarized current[J]. Nature, 2003, 425: 380-383.

[14] KAKA S, PUFALL M R, RIPPARD W H, et al. Mutual phase-locking of microwave spin torque nano-oscillators[J]. Nature, 2005, 437: 389-392.

[15] BRATAAS A, TSERKOVNYAK Y, BAUER G E W, et al. Spin battery operated by ferromagnetic resonance[J]. Phys Rev B, 2002, 66: 060404 .

[16] MORIYAMA T, CAO R, XIAO J Q. Magnetization reversal by microwave in magnetic tunnel junctions[J]. J Appl Phys, 2008, 103: 07A906.

[17] GUPTA K C, GARG R, BAHL I J. Microstrip lines and slotlines[M]. Boston-London: Artech House Publishers, 1996.

[18] VEYRES C, HANNA V F. Extension of the application of conformal mapping techniques to coplanar lines with finite dimensionsInt[J]. J Electron, 1980, 48(1): 47- 56.

[19] KUPFERSCHMIDT J N, ADAM S, BROUWER P W. Theory of the spin-torque-driven ferromagnetic resonance in a ferromagnet/normal-metal/ ferromagnet structure[J]. Phys Rev B, 2006, 74: 134416.

[20] KAKA S, RUSSEK S E. Precessional switching of submicrometer spin valves[J]. Appl Phys Lett, 2002, 80: 2958 .

[21] SUN Z Z, WANG X R. Strategy to reduce minimal magnetization switching field for Stoner particles[J]. Phys Rev B, 2006, 73(9): 092416 .

[22] ZHU J G, ZHU X C, TANG Y H, et al. Microwave-assisted magnetic recording[J]. IEEE Transactions on Magnetics, 2008, 44(1): 125-131.

[23] TSERKOVNYAK Y, BRATAAS A, BAUER G E W. Spin pumping and magnetization dynamics in metallic multilayers[J]. Phys Rev B, 2002, 66(22): 224403.

[24] TSERKOVNYAK Y, BRATAAS A, BAUER G et al. Nonlocal magnetization dynamics in ferromagnetic heterostructures[J]. Reviews of Modern Physics, 2005, 77(4): 1375.

[25] ZAFFALON M, B J van Wees, Spin injection, accumulation, and precession in a mesoscopic nonmagnetic metal island[J]. Phys Rev B, 2005, 71: 125401.

[26] SLAVIN A N, KABOS P. Approximate theory of microwave generation in a current-driven magnetic nanocontact magnetized in an arbitrary direction[J]. IEEE Transactions on Magnetics, 2005,41(4): 1264-1273 .

[27] WEI Z, SHARMA A, NUNEZ A S,[1] et al. Changing exchange bias in spin valves with an electric current[J]. Phys Rev Lett , 2007, 98(11): 116603.

[28] WU M C, AZIZ A, MORECTOFT D, et al. Spin transfer switching and low-field precession in exchange-biased spin valve nanopillars[J]. Appl Phys Lett, 2008, 92: 142501.

[29] KUBOTA H, FUKUSHIMA A, YAKUSHIJI K, et al. Quantitative measurement of voltage dependence of spin-transfer torque in MgO-based magnetic tunnel junctions[J]. Nat Phys, 2008, 4(1): 37-41 .

[30] TSERKOVNYAK Y, BRATAA A S, BAUER G E W. Enhanced gilbert damping in thin ferromagnetic films[J]. Phys Rev Lett, 2002, 88: 117601 .

[31] URBAN R, WOLTERSDORF G, HEINRICH B. Gilbert damping in single and multilayer ultrathin films: Role of interfaces in nonlocal spin dynamics[J]. Phys Rev Lett, 2001, 87: 217204 .

[32] HEINRICH B, WOLTERSDORF G, URBAN R, et al. Role of dynamic exchange coupling in magnetic relaxations of metallic multilayer films[J]. J Appl Phys, 2003, 93: 7545.

[33] LENZ K, TOLIŃSKI T, LINDNER J, et al. Evidence of spin-pumping effect in the ferromagnetic resonance of coupled trilayers[J]. Phys Rev B, 2004, 69, 144422 .

[34] MORIYAMA T. Nonlocal and local magnetization dynamics excited by an RF magnetic field in magnetic

multilayers[D]. Delaware: University of Delaware, 2008.
[35] WANG X H, GERRIT E, BAUER W, et al. Voltage generation by ferromagnetic resonance at a nonmagnet to ferromagnet contact[J]. Phys Rev Lett, 2006, 97: 216602 .
[36] COSTACHE M V, SLADKOV M, WATTS S M, et al. Electrical detection of spin pumping due to the precessing magnetization of a single ferromagnet[J]. Phys Rev Lett, 2006, 97: 216603.
[37] MORIYAMA T, CAO R, FAN X, et al. Tunnel barrier enhanced voltage signal generated by magnetization precession of a single ferromagnetic layer[J]. Phys Rev Lett, 2008,100: 067602.
[38] BRATAAS A, BAUER G E W, KELLY P J. Non-collinear magnetoelectronics[J]. Physics Reports, 2006, 427: 157.
[39] CHUI S T, LIN Z F. Large voltage from spin pumping in magnetic tunnel junctions[J] Phys Rev B, 2008, 77: 094432.

编　辑　张　俊

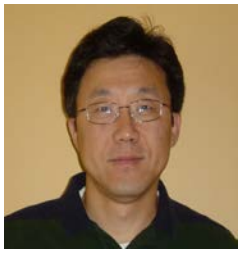

肖　强(John Q. Xiao)，美国Delaware大学教授，博士生导师，电子科技大学长江学者讲座教授。Delaware大学物理与天文系磁电实验室主任，自旋电子学与生物检测中心主任。1984年毕业于南京大学，1993年于美国琼斯·霍普金斯大学(Johns Hopkins University)获得博士学位并继续从事博士后研究工作，1995年成为特拉华大学助理教授，1999年获得国家自然科学基金海外青年学者合作研究基金，2005年晋升为Delaware大学全职正教授。主要研究领域为自旋电子学、微波材料与器件、凝聚态物理学等。肖强教授首次发现了颗粒膜中的巨磁阻效应，其论文在Phys. Rev. Lett. 发表，被引用次数已达1 200以上，成为“自旋电子学”的奠基性文献之一。他还是美国物理学会会员，美国材料研究学会会员和国际磁学和磁性材料会议顾问委员，多次担任国际美国物理协会磁性与磁性材料(MMM)大会分会主席，在各种国际会议上作邀请报告20多次，发表学术论文150多篇。